Eur. Phys. J. A **9**, 35–47 (2000)

THE EUROPEAN PHYSICAL JOURNAL A

Evolution of the N = 20 and N = 28 shell closures in neutron-rich nuclei

S. Péru, M. Girod[a], and J.F. Berger

CEA/DIF, DPTA/SPN, Boîte Postale 12, 91680 Bruyères-le-Châtel, France

Received: 26 July 2000
Communicated by P. Schuck

Abstract. The isospin dependence of shell closure phenomena is studied for light neutron-rich nuclei within a microscopic self-consistent approach using the Gogny force. Introducing configuration mixing, ^{32}Mg is found to be dynamically deformed, although the $N = 20$ spherical shell closure persists at the mean-field level for all $N = 20$ isotones. In contrast, the $N = 28$ spherical shell closure is found to disappear for $N - Z \geq 10$ whereas deformed shell closures are preserved and lead to shape coexistence in ^{44}S. Configuration mixing shows that the ground state of this nucleus is triaxially deformed. The first 2^+ excitation energy $E_x = 1.46$ MeV and the reduced transition probability $B(E2; 0^+_{\rm gs} \rightarrow 2^+_1) = 420\ e^2\,{\rm fm}^4$ obtained with our approach are in good agreement with experimental data.

PACS. 21.60.Ev Collective models – 21.60.Jz Hartree-Fock and random-phase approximations – 21.10.Re Collective levels and giant resonances – 21.10.Ky Static electromagnetic moments

1 Introduction

The numbers 2, 8, 20, 28,..., which represent the number of protons or neutrons of closed-shell spherical nuclei, have been interpreted with considerable success by the single-particle shell model [1]. Nowadays, these numbers are well reproduced by Hartree-Fock (HF) or Hartree-Fock-Bogoliubov (HFB) mean-field approaches, in which the nucleon-nucleon interaction is either taken as a parameterized effective force or modeled with meson exchange in a relativistic formalism. Magic numbers being associated with a shell closure, *i.e.* with a large energy gap between occupied and unoccupied single-particle levels, pairing correlations usually are weak or absent in the ground state (GS) of magic nuclei.

With the development of several radioactive beam experimental facilities, a new rich field of nuclear physics has been opening : the structure of nuclei far away from the valley of stability. Experimental data on exotic nuclei are of considerable interest for extending our knowledge of nuclear structure and for checking the theoretical models which have so far been used for normal nuclei. One open question in this context is whether magic numbers are universal, or whether they change or disappear in exotic regions, as they do for deformed nuclei.

One of the first investigation in this direction was the HF calculations performed by Campi *et al.* with the Skyrme interaction [2], for neutron-rich Na isotopes. The semi-magic nucleus ^{31}Na was found deformed, a result consistent with the mass measurement of Thibault *et al.* [3]. More generally, experimental mass measurements of $N = 20$ isotones yield S_{2n} curves that strongly indicate that the $N = 20$ magic gap vanishes in exotic nuclei [4–6]. One of the first theoretical study of excited states in ^{32}Mg, based on an interacting quasi-particle model [7], did not succeed in reproducing the very low excitation energy (E_x = 885 keV) of the first 2^+ state [8,9]. Early studies made by Wildenthal and Chung [10] demonstrated the "collapse" of the conventional shell-model approach in very neutron-rich Na and Mg isotopes. It was subsequently shown that neutron-rich isotopes in the vicinity of $N = 20$ required the inclusion of $f_{7/2}$ neutron states in the shell model space of active orbits [11–16]. Results obtained in ^{32}Mg are generally in good agreement with the experimental data, although conclusions concerning the size of the island of inversion, the role of intruder state or the resulting triaxial instability slightly depend on the detail of models. It must be noted that pure mean-field approaches [17–20] — including the present study — obtain too small a GS deformation in ^{32}Mg for explaining the low 2^+ excited state in this nucleus. Let us mention however that angular-momentum projection seems to lead to a much closer agreement with experiment [21].

The Finite Range Droplet Model (FRDM) [22] finds that ^{32}Mg is a deformed nucleus, but predicts that the $N = 28$ ^{44}S nucleus is spherical. On the other hand, measurements of the half-life of this latter nucleus [23,24] and of the $B(E2; 0^+_{\rm gs} \rightarrow 2^+)$ for exciting the lowest 2^+ state [25] strongly indicate that the ^{44}S GS is deformed. Mean-field approaches predict a nonzero GS deformation [26,

[a] e-mail: girod@bruyeres.cea.fr

27] or shape coexistence [28,29], whereas the shell model calculation of ref. [30] concludes that the $N = 28$ shell closure persists. These results, along with those obtained in this work will be discussed more thoroughly in sect. 3.2.2.

The present paper is devoted to the analysis of the evolution of nuclear structure in $N = 20$ and $N = 28$ isotones, in particular of shell closures, as one goes from the valley of stability to very neutron-rich nuclei. A preliminary account of this work has been presented earlier [31].

In a first step HFB calculations are performed for six nuclei in each of the $N = 20$ and $N = 28$ isotonic chains, using the effective interaction D1S proposed by Gogny [32,33]. Axial and triaxial nuclear shapes are envisaged. Let us mention that several of the studied nuclei are close to the neutron drip-line, and therefore the full HFB method must be used [34]. A configuration mixing technique based on the Generator Coordinate Method (GCM) with five degrees of freedom (β and γ vibrations plus rotations) has then been applied to all nuclei in order to derive the low-lying collective rotational-vibrational excited states and the associated ground-state correlations.

The mean-field HFB approach and the results obtained in the $N = 20$ and $N = 28$ isotonic chains are presented in sect. 2. The method employed for configuration mixing is described in sect. 3. Detailed configuration mixing results will be shown mainly for ^{32}Mg and ^{44}S, since correlations beyond the mean-field approximation are essential in these two nuclei. Conclusions of this work are gathered in sect. 4.

2 The mean-field approach

2.1 The constrained HFB method

In the constrained HFB theory, the deformed states $|\Psi_q\rangle$ of the nuclear system are assumed to be quasiparticle (qp) vacua (see, *e.g.*, refs. [35] and [33])

$$\begin{aligned} |\Psi_q\rangle &= \prod_i \eta_i\,|0\rangle, \\ \eta_i\,|\Psi_q\rangle &= 0\ ,\ \forall i, \end{aligned} \tag{1}$$

the quasiparticles η_i being defined via the general Bogolyubov transformation. The qp η_i states are deduced from the minimization of the energy functional

$$\delta\langle\Psi_q|\hat{H} - \lambda_N\hat{N} - \lambda_Z\hat{Z} - \sum_i \lambda_i\hat{Q}_i|\Psi_q\rangle = 0, \tag{2}$$

where $\hat{H}$ is the many-body nuclear Hamiltonian and the λ's are the Lagrange parameters associated with the constraints on nucleon numbers and average deformation parameters (see for example [36])

$$\begin{aligned} \langle\Psi_q|\hat{N}|\Psi_q\rangle &= N, \\ \langle\Psi_q|\hat{Z}|\Psi_q\rangle &= Z, \\ \langle\Psi_q|\hat{Q}_i|\Psi_q\rangle &= q_i. \end{aligned} \tag{3}$$

In this work, the $\hat{Q}_i$'s are taken as the quadrupole operators $\hat{Q}_{20}$ and $\hat{Q}_{22}$ that generate β- and γ-deformations, respectively. Equation (2) leads to the usual HFB equations, which we solve by iterative diagonalization of the HFB Hamiltonian

$$H_{\rm HFB} = \begin{pmatrix} e & \Delta \\ -\Delta^* & -e^* \end{pmatrix}, \tag{4}$$

where

$$e = h - \lambda_N\delta_{\tau,-1/2} - \lambda_Z\delta_{\tau,1/2}, \tag{5}$$

with

$$\begin{aligned} h_{\alpha\gamma} = \frac{(p)^2_{\alpha\gamma}}{2M}\left(1 - \frac{1}{A}\right) - \sum_i \lambda_i Q_i \\ + \sum_{\beta\delta}\langle\alpha\beta|V|\widetilde{\gamma\delta}\rangle\rho_{\delta\beta} \\ + 1/2\sum_{\alpha'\gamma'}\sum_{\beta\delta}\langle\alpha'\beta|\frac{\partial V}{\partial\rho_{\gamma\alpha}}|\widetilde{\gamma'\delta}\rangle\rho_{\gamma'\alpha'}\rho_{\delta\beta}, \end{aligned} \tag{6}$$

and

$$\Delta_{\alpha\beta} = \sum_{\gamma\delta}\langle\alpha\beta|V|\gamma\delta\rangle\kappa_{\delta\gamma}, \tag{7}$$

are the matrix elements of the mean-field Hamiltonian and of the pairing field, respectively. The quantities

$$\begin{aligned} \rho_{\alpha\beta} &= \langle\Psi_q|c^+_\beta c_\alpha|\Psi_q\rangle, \\ \kappa_{\alpha\beta} &= \langle\Psi_q|c_\alpha\ c_\beta|\Psi_q\rangle, \end{aligned} \tag{8}$$

represent the nuclear density matrix and pairing tensor, respectively.

In our approach, the many-body Hamiltonian $\hat{H}$ is assumed to include the term $-\frac{\langle\hat{P}^2\rangle}{2AM}$ that corrects the total energy for the spurious motion of the nucleus center-of-mass. Here $\vec{P} = \sum_i \vec{p}_i$ is the nucleus linear momentum and $A = N + Z$. This term leads to the one-body correction $\frac{-\hat{p}^2}{2M}\frac{1}{A}$ in h (eq. (6)), and to a two-body correction $\sum_{i\neq j} -\frac{\vec{p}_i\cdot\vec{p}_j}{AM}$ which is assumed to be included in the N-N interaction V. In the present work, V is taken as the D1S effective force of Gogny [32], whose parameters are given in [33,36]. This force is of finite range and therefore can be used to calculate both the mean-field Hamiltonian h and the pairing field Δ. This is also a density-dependent interaction, hence the $\partial V/\partial\rho$ term in eq. (6).

A number of studies [37] have shown that the Gogny force gives a realistic description of nuclear systems including the lightest nuclei.

The HFB equations are solved in triaxial symmetry, by keeping the parity and the z-signature of qp states as good quantum numbers [35]. The nuclear states $|\Psi_q\rangle$ are also assumed to be invariant under time-reversal symmetry $\mathcal{K}$ and under the transformation $\mathcal{K}\Pi_2$, where Π_2 is

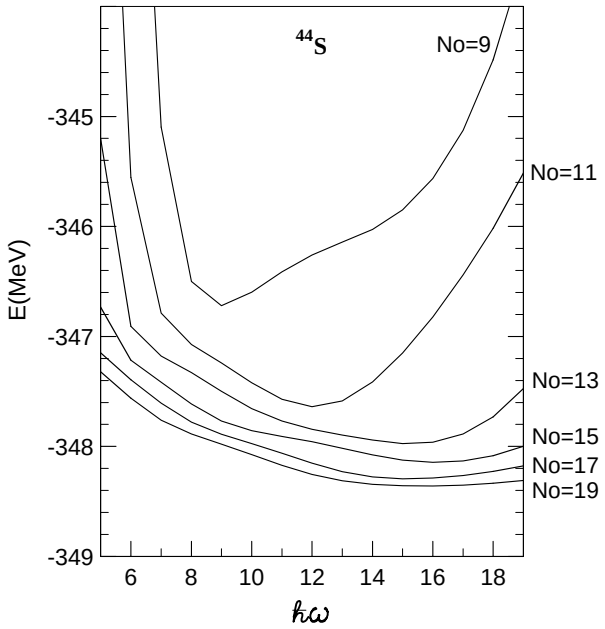

Fig. 1. HFB energies in spherical symmetry as functions of the harmonic oscillator parameter $\hbar\omega$ for bases with 9 to 19 major shells in ^{44}S.

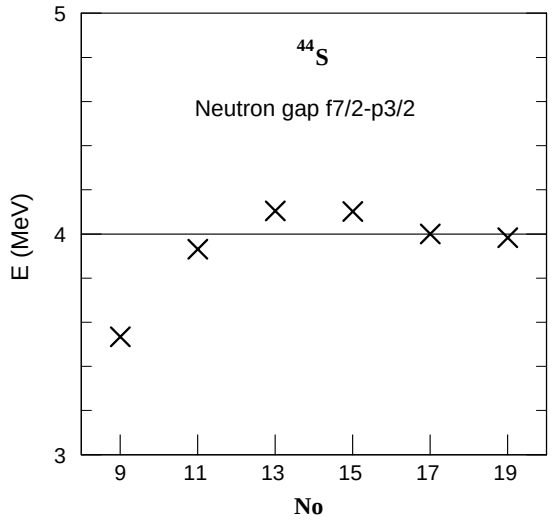

Fig. 2. Nilsson gap between the $d_{3/2}$ and $f_{7/2}$ levels as a function of the number (N_0) of oscillator shells in ^{44}S. For each N_0, the $\hbar\omega$ parameter is chosen in order to minimize the HFB energy.

the reflection with respect to the xOz plane. As a consequence, all matrix elements in the harmonic oscillator bases described below are real.

As in ref. [35], the qp states are expanded on triaxial harmonic oscillator bases. We have chosen bases including 11 major shells, which has been checked to be the smallest size providing a correct treatment of neutron-rich nuclei between $A = 30$ and $A = 54$. As an example, fig. 1 shows the HFB energy in spherical symmetry as a function of the the oscillator parameter $\hbar\omega$ for different numbers (N_0) of major shells in ^{44}S. One observes that $N_0 = 19$ can be considered as a an excellent approximation — within 200 keV — of an infinite basis. With the $N_0 = 11$ basis chosen here, the overestimation of the HFB energy is smaller than 1 MeV. In order to properly interpret shell closure phenomena, it is important to check that individual levels, particularly the relative location of the first empty level with respect to the Fermi level (*i.e.* the HF gap) are stabilized with respect to the basis parameters $\hbar\omega$ and N_0. We show in fig. 2 the neutron HF gap in ^{44}S as a function of N_0. The $\hbar\omega$ parameters have been chosen in order to minimize the HFB energy for each value of N_0. Their values are $\hbar\omega = 9$, 12, 15, 16, 15, 16 MeV for $N_0 = 9$, 11, 13, 15, 17, 19, respectively. All HF gap values are within ± 200 keV (except for $N_0 = 9$), and converge to 4 MeV. In the case of the $N_0 = 11$ basis adopted in present calculations, the relative error on the HF gap appears to be lower than 2%.

The total HFB energy can be written

$$\mathcal{E} = \mathrm{Tr}[\frac{p^2}{2M}\left(1 - \frac{1}{A}\right)\rho] + \frac{1}{2}\mathrm{TrTr}V\rho\rho + \frac{1}{2}\mathrm{Tr}\Delta\kappa. \quad (9)$$

The last term is the pair correlation energy, which we will call here pairing energy. Let us emphasize that this pairing energy differs from the net gain in binding energy brought by pairing correlations (see, *e.g.*, ref. [32]).

In the following, it will be convenient to adopt the Bohr coordinates:

$$\beta = \sqrt{\frac{\pi}{5}}\frac{\sqrt{(q_{20}^2 + 3q_{22}^2)}}{AR^2} \quad \text{and} \quad \gamma = \arctan\frac{\sqrt{3}q_{22}}{q_{20}}, \quad (10)$$

instead of the deformation parameters q_{20} and q_{22}. The radius R is given by

$$R^2 = \frac{3}{5}\left(1.2A^{1/3}\right)^2 \text{ fm}^2, \quad (11)$$

a definition slightly different from the one adopted in ref. [35].

2.2 Results

In order to better discuss our results and to compare them with those of other works, we will make use of the following definition of shell closures. We will consider that a shell closure occurs when three conditions are met : i) the nuclear energy is minimum, ii) there is a significant gap above the Fermi level, and iii) pairing correlations vanish. The last condition actually will allow us to give a quantitative meaning to what we will consider as a "significant" single-particle gap. This definition will be employed for spherical as well as deformed nuclei. As for the magic numbers, we will associated them only with spherical shell closures. In this sense, the scope of this work is not restricted to the magic numbers $N = 20$ and $N = 28$, since we intend to look at the more general phenomenon of shell closures and their change as $N - Z$ evolves.

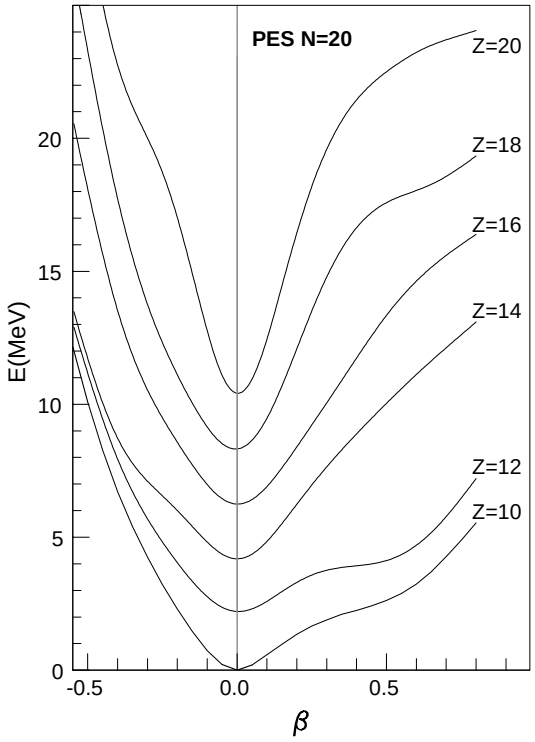

Fig. 3. Potential energies curves of the $N = 20$ isotones, as functions of the axial deformation parameter β. The minima of the curves are arbitrarily separated by 2.1 MeV.

2.2.1 The $N = 20$ shell

In order to study the evolution of the $N = 20$ shell closure, constrained HFB calculations have been performed for the $N = 20$ even isotones having Z equal to 20,18,16,14,12 and 10. Let us note that ^{30}Ne is the last even-even $N = 20$ nucleus to be bound before the neutron drip-line is reached, since $^{28}_{8}O_{20}$ is unbound [38].

The potential-energy surfaces (PESs) of ^{40}Ca, ^{38}Ar, ^{36}S, ^{34}Si, ^{32}Mg, and ^{30}Ne as functions of the axial deformation parameter β are plotted in fig. 3. One notices that all the PESs have a minimum at $\beta = 0$. In other words, the GSs of these $N = 20$ isotones are spherical within the HFB approximation. This result validates the above first condition for a spherical shell closure. However, the softness of the PESs increases with increasing $N - Z$. The doubly magic nucleus ^{40}Ca is the most rigid against β-deformation. ^{32}Mg, the softest of the six nuclei, displays a shallow secondary minimum (a few keV deep) at $\beta \simeq 0.4$. This result is consistent with those obtained with other mean-field approaches [17–20]. Let us note that ^{30}Ne is also found to be quite soft.

In order to check the second condition needed for a spherical shell closure, we display in fig. 4 the individual neutron levels around the Fermi sea at $\beta = 0$ for the six isotones.

The single-particle energies are defined as the eigenvalues of the Hamiltonian h, eq. (6). These eigenvalues have been checked to be practically identical to the diagonal values of the Hamiltonian h transformed to the HFB canonical basis. This is so because the pairing field Δ of eq. (7) practically vanishes at sphericity (see below). Two distinct features emerge from these level sequences. First, the energy difference between the last occupied level($d_{3/2}$), the Fermi level, and the first empty level ($f_{7/2}$) decreases from 7.02 MeV for Ca down to 5.37 MeV for Ne.

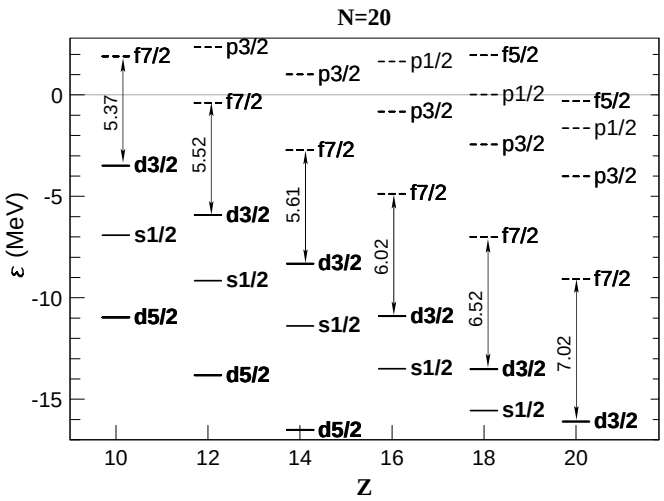

Fig. 4. Energies of spherical neutron individual levels of $N = 20$ isotones as functions of the number of protons. Empty levels are drawn with dash lines and occupied levels with solid lines. Labels indicate the spherical quantum numbers lj. Values near the arrows give the Nilsson gap in MeV of each element.

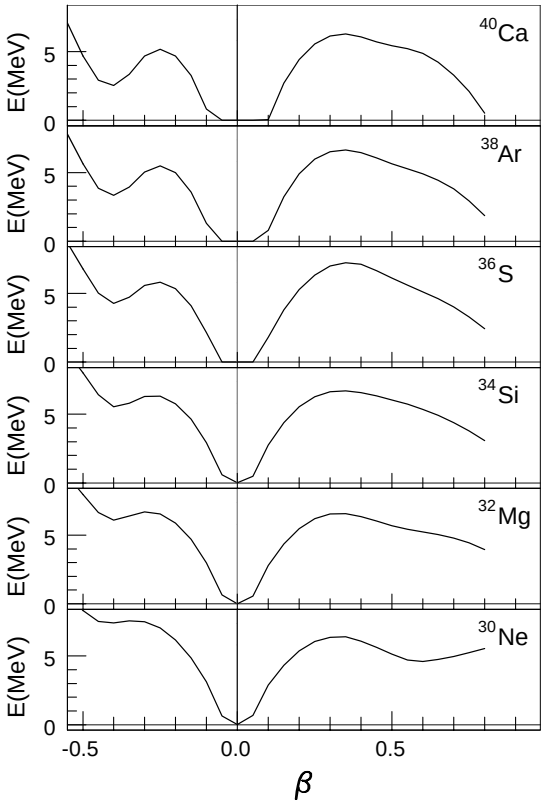

Fig. 5. Neutron pairing energies of the even $N = 20$ isotones with even $Z = 10$ to 20, as functions of the axial deformation parameter β.

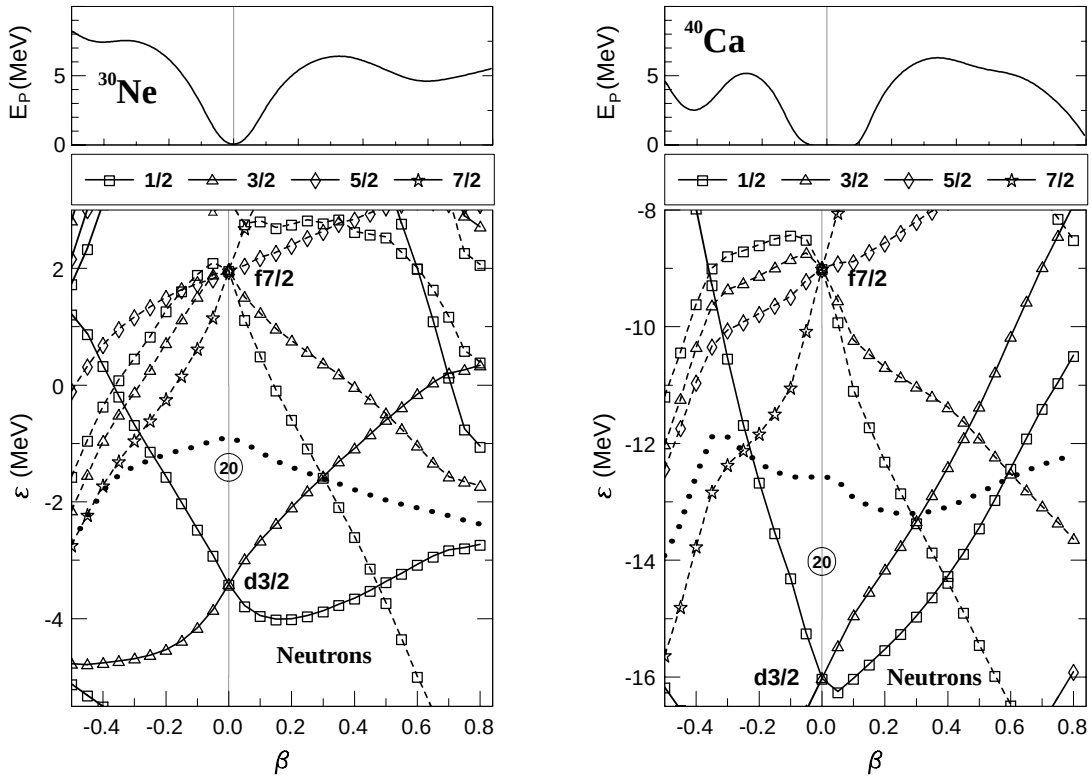

Fig. 6. Bottom: Neutron single-particle levels close to the Fermi surface for ^{30}Ne (left) and ^{40}Ca (right), as functions of the axial deformation parameter β. Levels with positive and negative parities are shown as solid and dashed lines, respectively. The dotted lines represent the values of the chemical potential. Top: neutron pairing energies.

Therefore, the $N = 20$ spherical shell gap weakens as $N-Z$ increases. Nevertheless, it remains strong enough to preserve the magic character of the $N = 20$ shell. Finally, the single-particle energies increase with $N - Z$. In particular, for ^{30}Ne the $f_{7/2}$ energy becomes positive (1.96 MeV). This indicates that ^{30}Ne is close to the neutron drip-line.

In order to check the third condition, *i.e.* the vanishing of pairing correlations, we show in fig. 5 the neutron pairing energy of the six nuclei as a function of the axial deformation parameter β. These curves illustrate the change in the "structure" of the $N = 20$ shell closure as a function of $N - Z$ and deformation. We observe that the pairing energy of all the isotones vanishes at $\beta = 0$ in the same way as in the $N = Z = 20$ ^{40}Ca nucleus, which can be considered as a reference in this respect. Therefore, the $N = 20$ gap in the single-particle levels is large enough to be associated with a spherical shell closure.

Additional information can be extracted from these curves concerning the influence of deformation. As can be seen, the pairing energy vanishes only in a small range of deformation around the spherical shape. This behaviour signs the pure spherical nature of the $N = 20$ shell closure. The fact that the pairing energies increase more rapidly with deformation when the proton-neutron difference increases is correlated with the relative softness of the potential for the most exotic nuclei. One could say that, in the HFB description, the pairing correlations reduce the energy loss due to deformation. The prolate pairing maximum is roughly identical for all nuclei, while the oblate one tends to increase with $N - Z$.

As expected, pairing energies are strongly correlated with level sequences. As an example, fig. 6 shows the individual neutron energy levels obtained from the diagonalization of h (eq. (6)) and, in the uppermost part, the neutron pairing energy as functions of β-deformation in the case of ^{40}Ca and of the most exotic isotone, ^{30}Ne. In both cases, a significant $N = 20$ gap exists near $\beta = 0$.

The strong decrease of the ^{40}Ca pairing energy for $\beta > 0.7$, can be correlated with a Super Deformed (SD) Nilsson gap, larger than 3 MeV, occurring between the $3/2^-$ state coming from the $f_{7/2}$ spherical shell, and the $1/2^+$ state coming from the $d_{3/2}$ one. This SD gap can be associated with the SD shoulder in the PES of ^{40}Ca (see fig. 3). For ^{30}Ne, this gap does not exist, but another gap 3 MeV wide, appears between the $1/2^-(f_{7/2})$ and $3/2^+(d_{3/2})$ levels. This gap is only 2 MeV wide in ^{40}Ca. Its presence explains the minimum in the pairing energy at $\beta = 0.55$. However, it is not large enough to cancel out pairing correlations and, therefore, to constitute a (deformed) shell closure in the sense given earlier. For oblate deformations, the pairing energy minimum at $\beta = -0.4$ increases from 2.5 MeV for ^{40}Ca up to 7 MeV for ^{30}Ne (see fig. 5). This minimum is associated with a HF gap between the $7/2^-$ and $5/2^-$ levels from the $f_{7/2}$ shell, which decreases from 3 MeV in ^{40}Ca to less than 1

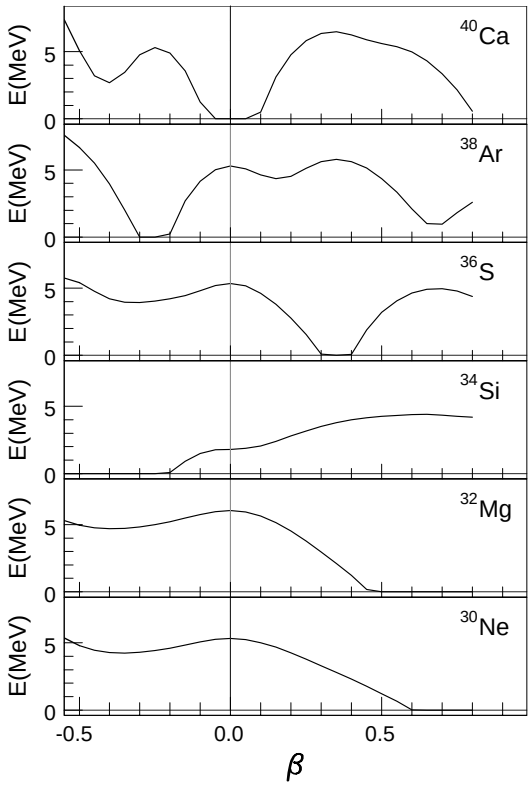

Fig. 7. Proton pairing energies of the studied even $N = 20$ isotones, as functions of the axial deformation parameter β.

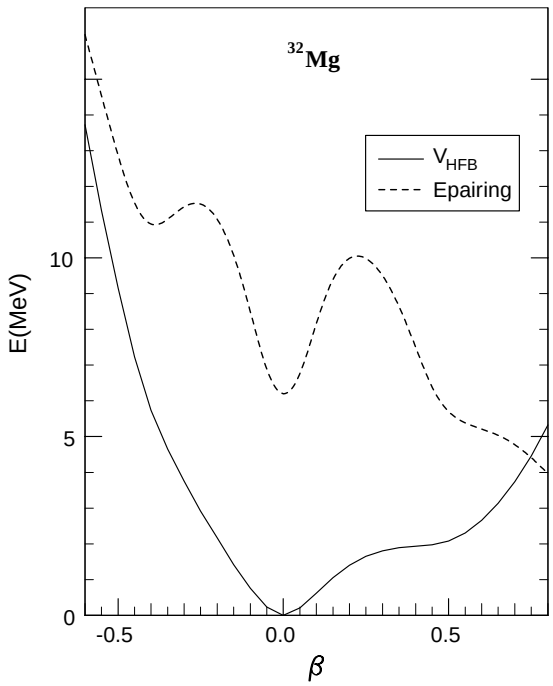

Fig. 8. Proton plus neutron pairing energy (Epairing) and HFB potential ($V_{\rm HFB}$) in ^{32}Mg as functions of β.

MeV in ^{30}Ne. These remarks show that the neutron level scheme as a function of deformation, strongly depends on the $N - Z$ difference.

Thus, the $N = 20$ spherical shell closure is preserved within the present mean-field approach, even if the proton neutron difference tends to weaken the magnitude of this shell closure.

In fig. 7 the pairing energies for protons are plotted as functions of β-deformation. As expected, the proton pairing correlations strongly differ from one element to the next one. If we leave aside the special case of the double magic nucleus ^{40}Ca, the proton pairing correlations are seen to almost vanish in ^{38}Ar for $-0.3 < \beta < -0.2$, and in ^{36}S for $0.3 < \beta < 0.4$. In ^{34}Si, the pairing energy is zero for $\beta < -0.2$.

These variations are consistent with the shoulders observed in the PESs of fig. 3. In fact, the deformation regions where pairing correlations vanish correspond to comparatively large HF gaps in the single-particle level schemes and therefore to an increased binding energy.

In the case of ^{32}Mg, the proton pairing energy begins to decrease at $\beta = 0.1$ and vanishes for prolate shapes with $\beta > 0.5$. This is due to a deformed shell effect occurring at $Z = 12$ which is associated with the secondary minimum of the PES at $\beta \simeq 0.6$. This deformed shell effect will be discussed in more detail below. For ^{30}Ne, the proton shell effect is present but less pronounced than for ^{32}Mg.

As an example of the relationship between shell effects, pairing correlations and PES minima, the sum of proton and neutron pairing energies, and the HFB energy of ^{32}Mg are drawn together in fig. 8, while proton and neutron single-particle levels are shown in fig. 9.

From these curves, it appears that there is a close correspondence between the PES variations and those of the pairing energy. While the spherical minima are due to a neutron shell effect, the prolate ones come from the large proton HF gap (5 MeV) at $\beta = 0.6$ (see fig. 9). Therefore the variations of the PES depend to a large extent on shell effects, which in turn strongly affect the magnitude of pairing correlations.

The $N = 20$ shell appears strong enough to stabilize spherical GSs, while proton shell effects act on the deformation properties of each nucleus. This is true at the mean-field level but as we will see next, this statement will have to be revisited when effects beyond the mean field are taken into account. Actually, the softness of some of the potential energy curves indicates that the corresponding nuclei have to be described using mixings of constrained HFB states.

2.2.2 The $N = 28$ shell

In order to analyze the $N = 28$ shell in the same manner as the $N = 20$ one, we have performed constrained HFB calculations for six $N = 28$ isotones. The three previous conditions needed to verify the occurrence of a shell closure will be checked one by one.

Figure 10 shows the PESs as functions of the axial parameter β for the six studied isotones: ^{42}Si, ^{44}S, ^{46}Ar, ^{48}Ca, ^{50}Ti and ^{52}Cr. ^{52}Cr is on the line of β-stability and will be considered as a reference nucleus. Unlike for the

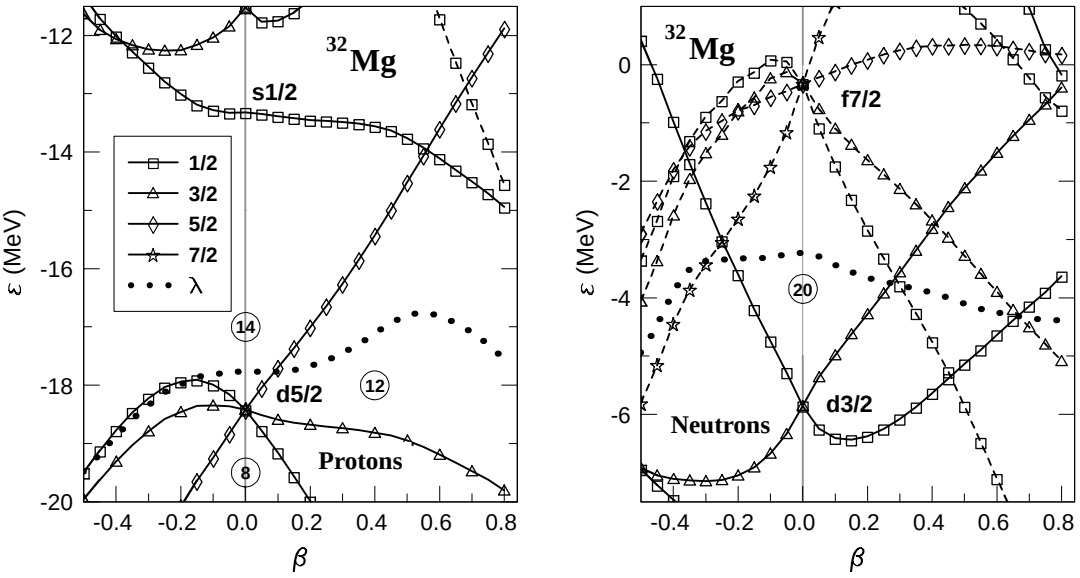

Fig. 9. Single-particle levels for proton (left) and neutron (right) in ^{32}Mg. Levels with positive and negative parities are shown as solid and dashed lines, respectively. The dotted lines represent the values of the chemical potentials.

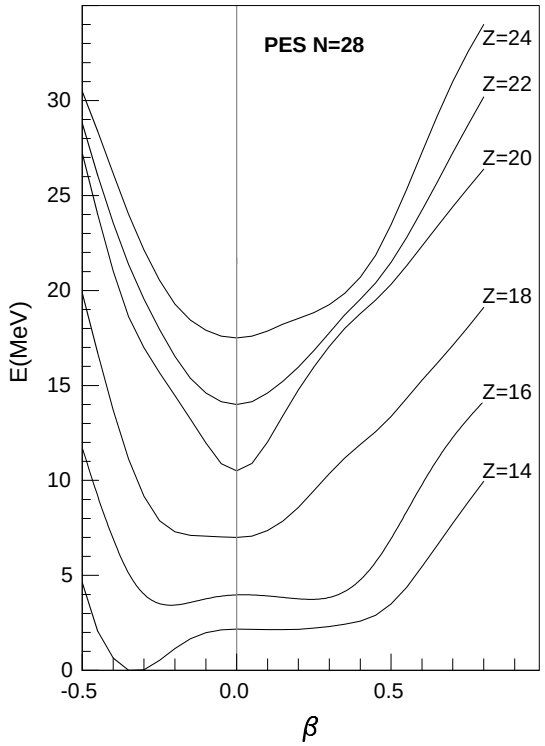

Fig. 10. Potential energies curves of the $N = 28$ isotones, as functions of the axial deformation parameter β. The minima of the curves are arbitrarily separated by 3.5 MeV.

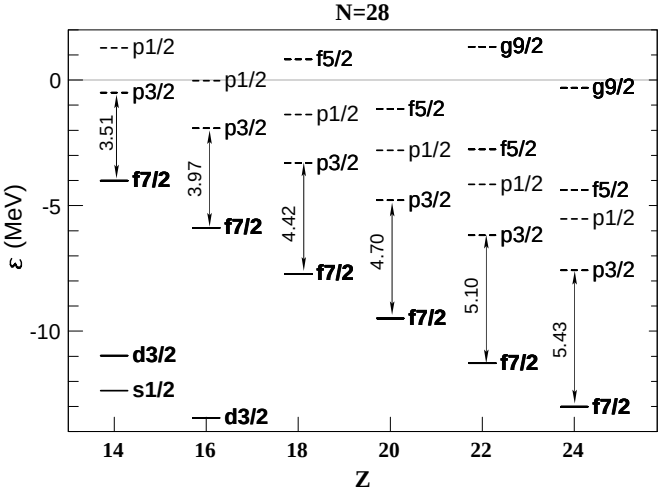

Fig. 11. Energies of spherical neutron individual levels of $N = 28$ isotones as functions of the number of protons. Empty levels are drawn with dash lines and occupied levels with solid lines. Labels indicate the spherical quantum numbers lj. Values near the arrows give the Nilsson gap in MeV of each element.

$N = 20$ shell, only three nuclei (^{48}Ca, ^{50}Ti and ^{52}Cr) display spherical GSs. ^{48}Ca being doubly magic is the most rigid of all six nuclei. For ^{46}Ar, the GS corresponds to the very shallow oblate minimum near $\beta = -0.25$. For ^{42}Si, the PES exhibits an oblate 2 MeV deep GS minimum at $\beta \simeq -0.3$. For ^{44}S, the PES displays two minima: an oblate one at $\beta = -0.2$ and a prolate one at $\beta = 0.3$. The β-γ PES of this nucleus (see fig. 17) shows that these minima are genuinely axial ones, *i.e.*, they are not connected by any triaxial valley. The two minima have relatively small depths : 230 keV for the prolate well and 520 keV for the oblate one. This is in agreement with the study of Werner *et al.* [28,27], in which a shape coexistence has been identified. This result is also found with the RMF calculation of ref. [29]. The absence of any spherical HFB minima in Ar, S, and Si shows that the $N = 28$ spherical shell closure is broken, since the first of the above conditions is not fulfilled.

Figure 11 shows the individual energy levels at sphericity for all six nuclei. The $N = 28$ HF gap between the $f_{7/2}$ and the $p_{3/2}$ levels decreases with decreasing Z, from 5.44 MeV for ^{52}Cr down to 3.5 MeV for ^{42}Si. The breaking of the $N = 28$ shell, which occurs between ^{46}Ar and ^{48}Ca corresponds to a $N = 28$ gap that becomes lower than about 4.5 MeV. This number therefore appears as the minimum gap value required to preserve the shell closure. Comparing with the previous $N = 20$ isotones, let us note that the most exotic nuclei ^{30}Ne$_{20}$ and ^{42}Si$_{28}$ in the two chains have the same value 1/3 for the asymmetry parameter $\delta = (N - Z)/A$. However, the HF gap in the $N = 28$ isotones are 1.6 to 1.5 MeV less than in the $N = 20$ nuclei. Therefore, $N = 28$ appears more as a sub-shell compared to the $N = 20$ shell. This observation explains why the $N = 28$ shell closure is more easily broken as $N - Z$ increases.

The neutron pairing energies displayed in fig. 12 as functions of β allow us to check the third condition mentioned above for the occurrence of the $N = 28$ shell closure. For ^{52}Cr, the neutron pairing energy indeed vanishes for $\beta = 0$, but also in the whole range $-0.4 < \beta < +0.1$, and at $\beta \simeq 0.4$ too. Therefore, the $N = 28$ shell closure is not only a magic spherical one but also a deformed one. Clearly, the variations of the pairing energy of the $N = 28$ isotones are very different from those of the $N = 20$ chain. The most striking feature is the stability of the deformed shell effects at $\beta \simeq 0.5$ and $\beta \simeq -0.3$ as $N - Z$ increases.

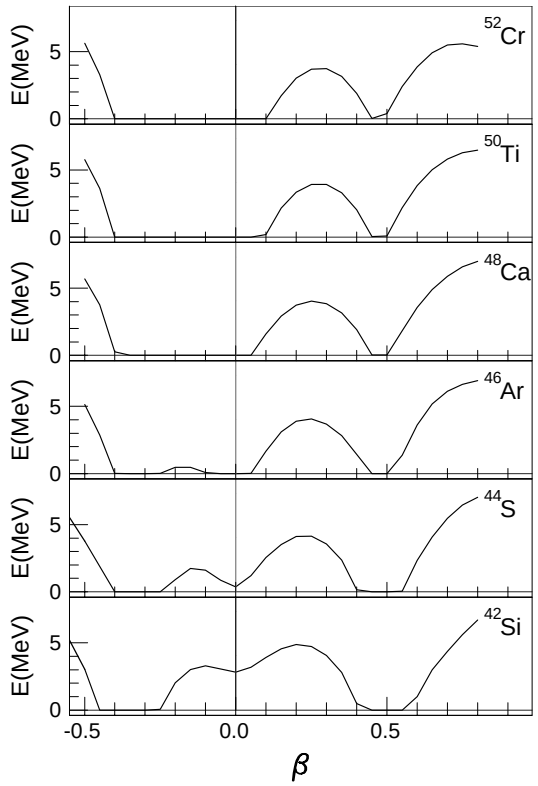

Fig. 12. Neutron pairing energies of the even $N = 28$ isotones with even $Z = 14$ to 24, as functions of the axial deformation parameter β.

On the other hand, the neutron pairing energy at $\beta = 0$, which vanishes for $Z = 18$–24, is 0.4 MeV for ^{44}S and 2.8 MeV for ^{42}Si. Therefore, while the spherical shell closure disappears for the most exotic $N = 28$ nuclei, strong shell effects exist at large prolate and oblate deformations. In order to understand the origin of these deformed shell effects, we display in fig. 13 the neutron individual levels for ^{42}Si and ^{52}Cr as functions of β. The prolate shell effect comes from a gap between the $7/2^-$ ($f_{7/2}$) level and the $1/2^-(p_{3/2})$ one, that covers a larger range of deformation ($0.2 < \beta \leq 0.8$) in ^{42}Si than in ^{52}Cr. Conversely, the oblate shell effect, which originates from a gap between the same levels as the spherical one, is stronger in ^{42}Si than in ^{52}Cr.

In order to get an idea of proton shell effects, we have drawn in fig. 14 the proton pairing energies of the $N = 28$ isotones. The curves are almost identical to those obtained for the $N = 20$ isotones (see fig. 7). For Cr and Ti, the proton pairing energy is non-zero in the whole range of deformations. Therefore, these elements do not have strong proton shell effects, which is consistent with the relative softness of the PESs. In the case of ^{48}Ca, it is important to note that the $Z = 20$ spherical shell closure appears as a strong one. For ^{46}Ar, oblate shapes compete with spherical ones due to a proton shell effect for $\beta < 0$.

The stronger proton shell effects occur for the exotic ^{44}S and ^{42}Si. In ^{44}S, the proton pairing energy vanishes in the whole range $0.25 < \beta < 0.45$, which explains the secondary minimum and the softness of the PES for prolate deformation. In fact, the proton shell effect occurs at deformations for which a large neutron shell effect is also present. The behaviour of the proton pairing energy in ^{42}Si confirms that this nucleus may be considered as a kind of doubly magic nucleus (see above). Pairing correlations vanish for a large range of oblate deformations ($\beta < -0.2$) which explains the oblate GS minimum at $\beta \simeq -0.3$. We observe that the proton pairing energy in ^{34}Si ($N = 20$) is globally larger than in ^{42}Si ($N = 28$). This is an indication of the effect of neutron excess on the proton level scheme.

To summarize, the *spherical* $N = 28$ shell closure is not preserved for exotic nuclei with $N - Z \geq 10$ in the sense of usual spherical shell closures, because the three conditions we have proposed are not all verified. On the other hand, deformed shell closures appear for these nuclei. In particular, the ground-state of ^{42}Si is found to be deformed, with large proton and neutron HF gaps and zero pairing. This result is consistent with the conclusion of Cottle and Kemper [39] who suggest that ^{42}Si " behaves in a doubly magic fashion ". A similar conclusion is reached by Retamosa *et al.* [30] from calculated S_{2n}'s. It is important to note that proton shell effects have a strong influence on the PESs of neutron-rich nuclei, especially when they are in combination with a neutron shell effect.

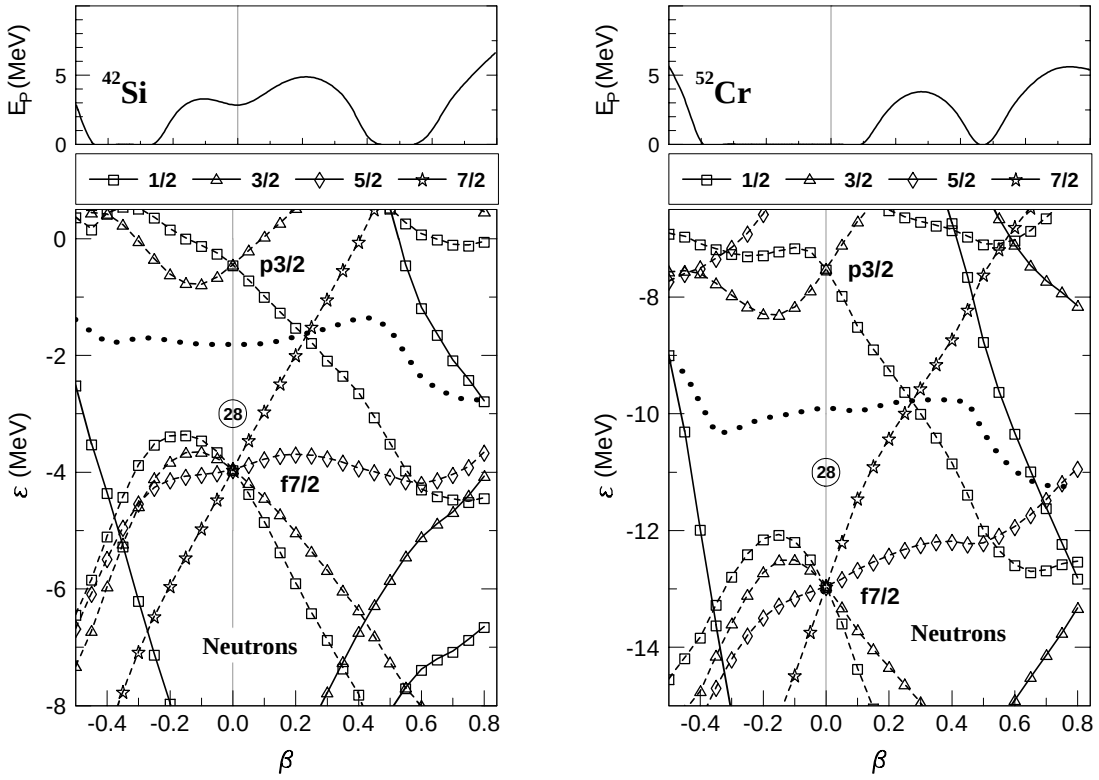

Fig. 13. Bottom: Neutron individual levels close to the Fermi surface of ^{42}Si (left) and ^{52}Cr (right) nuclei, as function of the axial deformation parameter β. Levels with positive and negative parities are shown as solid and dashed lines, respectively. The dotted lines represent the values of the chemical potential. Top: neutron pairing energies.

3 Beyond the mean field

In the previous section, we have shown that, at the mean-field level, the $N = 28$ spherical shell closure is spontaneously broken for $Z \leq 16$, while $N = 20$ remains a spherical magic number. This latter result appears to contradict experimental data which seems to indicate that the $N = 20$ shell closure disappears in neutron rich nuclei, particularly in ^{32}Mg. However, as we have seen, several $N = 20$ PESs show that differently deformed HFB configurations have close enough potential energies to be mixed by the residual interaction. In the present section, we examine the possible influence of such configuration mixings on the GS structure of the $N = 20$ and $N = 28$ nuclei, using a " dynamical " approach based on the Generator Coordinate Method (GCM). At the same time, we will obtain the $\pi = +$ low-lying rotational-vibrational collective levels, as explained in the next subsection.

3.1 The method

We assume the nuclear states are configuration mixings of constrained HFB wave functions, in the form given by the GCM theory [40]:

$$|\Phi_i\rangle = \int \mathrm{d}q \; |\Psi_q\rangle f_i(q). \qquad (12)$$

Here q is a multi-dimensional generator coordinate, which we take as $q = (\beta, \gamma, \theta_1, \theta_2, \theta_3)$, where (β, γ) are the usual Bohr quadrupole deformation parameters, and $(\theta_1, \theta_2, \theta_3)$ the three Euler angles.

A variational principle applied to the energy calculated with eq. (12) shows that the weight function $f_i(q)$ is a solution of the Hill-Wheeler equation [41] :

$$\int \mathrm{d}q' \left(H(q,q') - E_i I(q,q')\right) f_i(q') = 0, \qquad (13)$$

where $H(q,q') = \langle\Psi_q|\hat{H}|\Psi_{q'}\rangle$ and $I(q,q') = \Psi_q|\Psi_{q'}\rangle$ are the GCM energy and norm kernels, respectively, and E_i the energy associated with $|\Phi_i\rangle$.

Instead of solving eq. (13), we will here use the Gaussian overlap approximation (GOA) [42,43]. With this hypothesis, eq. (13) can be transformed into a new equation:

$$\hat{\mathcal{H}}_{\mathrm{coll}} g_i(q) = E g_i(q), \qquad (14)$$

where q is the above five degrees of freedom, and $g_i(q)$ the Gauss transform of $f_i(q)$. The collective Hamiltonian $\hat{\mathcal{H}}_{\mathrm{coll}}$ writes:

$$\hat{\mathcal{H}}_{\mathrm{coll}} = \frac{\hbar^2}{2}\sum_{k=1}^{3}\frac{\hat{I}_k^2}{\mathcal{J}_k} - \frac{\hbar^2}{2}\sum_{m,n=0,2} D^{-\frac{1}{2}}\frac{\partial}{\partial a_m} D^{\frac{1}{2}} {B_{mn}}^{-1}\frac{\partial}{\partial a_n}$$

$$+V(q) + \Delta V(q). \qquad (15)$$

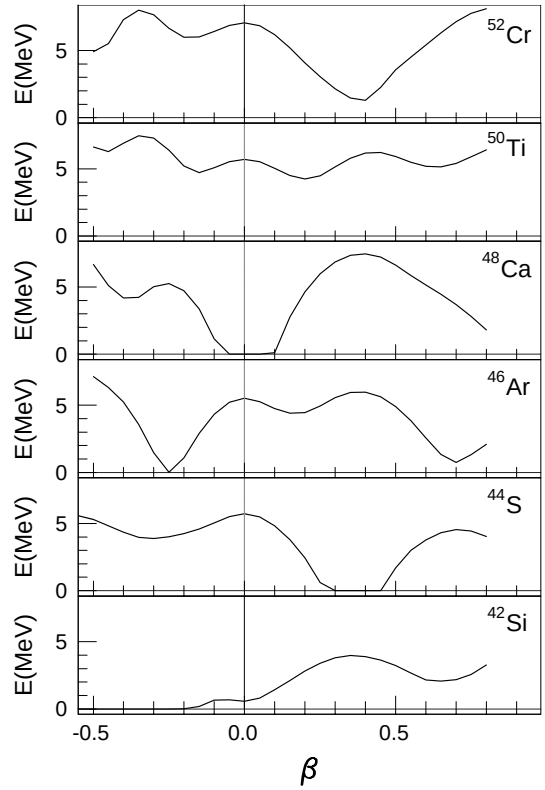

Fig. 14. Proton pairing energies for the studied even $N = 28$ isotones, as functions of the axial deformation parameter β.

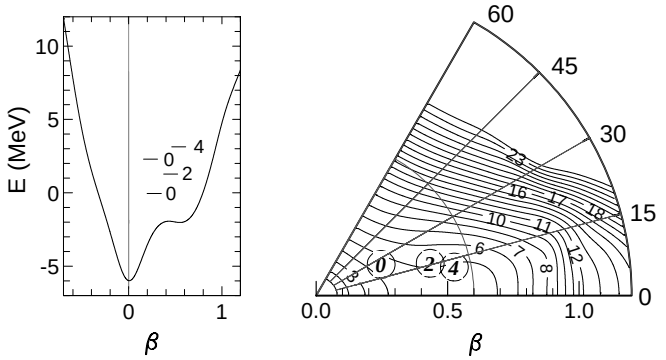

Fig. 15. Axial (left) and triaxial (right) potential energy surfaces of ^{32}Mg. The energy of the quadrupole collective levels is displayed in the left part. The circles in the β-γ right plot indicate the mean deformation of the first 0^+, 2^+ and 4^+ levels. Equipotential lines are shown in 1 MeV intervals.

with $a_0 = \beta\cos\gamma$, $a_2 = \beta\sin\gamma$, $V(q) = H(q,q)$, and $\Delta V(q)$ represents a 5-D zero point energy corrections (ZPE) (see ref. [44]). The kinetic term of the collective Hamiltonian includes collective inertia of vibrational type B_{mn} and the moments of inertia $\mathcal{J}_k$ of the rotational part. In this expression, $\widehat{I}_k$ is the k-component of the total angular momentum $\vec{I}$ in the intrinsic system, and

$$D = \left(B_{00}B_{22} - B_{02}^2\right)\prod_k \mathcal{J}_k \qquad (16)$$

is the determinant of the metric in the 5-D quadrupole collective space.

The eigenstates of $\hat{\mathcal{H}}_{\rm coll}$ may be expressed in terms of the coordinates (β,γ) as

$$|IM\rangle = \sum_{K=0}^{I} g_K^I(\beta,\gamma)\ |IMK\rangle.$$

Here, $|IMK\rangle$ is a normalized combination of Wigner rotation matrices, where M and K are the projections of the angular momentum $\vec{I}$ onto the third axis in the laboratory and intrinsic frames, respectively. Furthermore, $g_K^I(\beta,\gamma)$ is the vibrational collective wave function.

The inertia parameters B_{mn} are obtained here from the HFB wave functions using the Inglis approximation [45]. The rotational moments of inertia $\mathcal{J}_k$ have been derived in a self-consistent manner from full cranked HFB calculations [46]. More precisely, for each deformation, we minimize $\langle H - \omega_z J_z\rangle$ for a very small rotational frequency ω_z, which gives $\mathcal{J}_z = \langle J_z\rangle/\omega_z$. $\mathcal{J}_x$ and $\mathcal{J}_y$ are calculated using the same method with axis permutations. By solving eq. (14), a correlated GS is obtained, together with collective rotational-vibrational excited levels [47,48]. From the corresponding collective wave functions, we determine the average values $\langle\beta\rangle = \langle IM|\beta|IM\rangle$ and $\langle\gamma\rangle = \langle IM|\gamma|IM\rangle$ for ground and excited states and transition probabilities.

3.2 Results

In order to give an idea of the effects of configuration mixing in the description of the nuclear structure of exotic nuclei, we present results for two nuclei: $^{32}_{12}$Mg$_{20}$ and $^{44}_{16}$S$_{28}$. We have chosen these nuclei for two reasons. First, the topology of their potential energy surfaces shows that they are the most likely candidates for shape coexistence or configuration mixing. Second, recent experimental results exist for these two very exotic nuclei.

3.2.1 The ^{32}Mg nucleus

As we will show, although the $N = 20$ closure is preserved within the mean-field description, taking into account correlations associated with vibration-rotation modes induces a permanent GS deformation in ^{32}Mg.

Figure 15 shows the PES (with ZPE corrections included) of ^{32}Mg. In the right part of the figure, the PES is shown in the β-γ plane. The average deformations, $\langle\beta\rangle$ and $\langle\gamma\rangle$, and spins of the first collective levels are indicated by the circles. The cut of the PES along the axial directions $\gamma = 0°$ and $\gamma = 60°$ is shown in the left part of the figure together with the excitation energies and average β deformations (counted as positive) of the collective levels. From these two figures, one can see that the GS energy is large enough for the GS wave function to spread over the two wells of the PES. This can be seen in the upper part

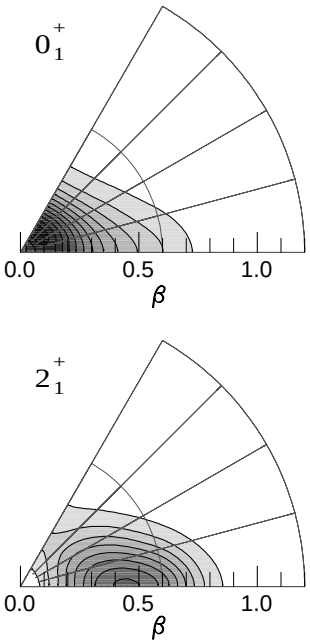

Fig. 16. Collective wave functions in β-γ plane of the first 0^+ and 2^+ collective levels of ^{32}Mg.

of fig. 16 which shows the GS collective wave function. The lower part of the same figure shows that the wave function of the first 2^+ state is well deformed ($\langle\beta\rangle = 0.45$) and peaked at large prolate deformation $\beta = 0.45$.

In agreement with experimental information, we therefore find that ^{32}Mg is a deformed $N = 20$ nucleus. The first 2^+ and 4^+ are 98% $K = 0$, which indicates that they can be considered as members of a rotational band. The excitation energy of the first 2^+ is very small (1.32 MeV) in comparison with usual closed shell nuclei ($\sim$ 3 MeV). Nevertheless, this energy is still too large compared with the experimental value (0.885 MeV). This disagreement seems to be due to too small a mean deformation of the band head. Let us note that the drift in the GS band deformation is quite large since $\langle\beta\rangle$ increases from 0.274 for the 0^+ level to 0.536 for the 4^+ level. It is instructive to compare the theoretical moment of inertia $\mathrm{J}_I^{(1)} = (2I-1)/(E_I - E_{I-2})$ of the $2_1^+ \rightarrow 0_{\rm gs}^+$ and $4_1^+ \rightarrow 2_1^+$ transitions with the $2_1^+ \rightarrow 0_{\rm gs}^+$ experimental one. We find 2.29 and 3.78 $\hbar^2\,\mathrm{MeV}^{-1}$ for the 2^+ and 4^+, respectively, whereas the 2^+ experimental value is 3.38 $\hbar^2\,\mathrm{MeV}^{-1}$. Clearly, a more deformed (therefore less bound) GS would give a better agreement with experiment for the 2^+ excitation energy. This could possibly be obtained by taking into account other degrees of freedom, as the octupole mode or higher multipole deformations. Nevertheless, the deformation of collective levels is strongly correlated to the behaviour of inertia parameters. In our approach, these parameters are obtained in the Inglis approximation. We think that a more consistent calculation, especially in the situation where strong shell effects are present, would probably improve our results, as indicated by preliminary calculations [49]. A second 0^+ level is found at 2.35 MeV excitation energy. Note that in fig. 15, the first and the second minima of the PES are more pronounced than in fig. 3 because ZPE corrections are included.

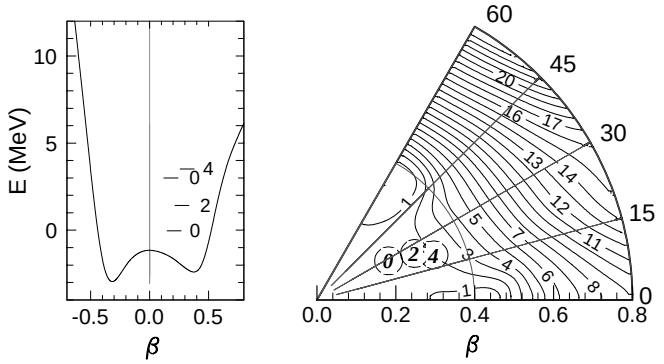

Fig. 17. Same as fig. 15 for ^{44}S.

The experimental $B(E2; 0_{\rm gs}^+ \rightarrow 2_1^+)$ has been measured by Motobayashi using radioactive beams in RIKEN [50] and via intermediate energy Coulomb excitation by Prity-chenko [51]. When feeding corrections are included, a value of 333 (70) $e^2\,\mathrm{fm}^4$ is obtained, which is well reproduced in our approach, which gives $B(E2; 0_{\rm gs}^+ \rightarrow 2_1^+) = 333.5$ $e^2\,\mathrm{fm}^4$. The fact that our $B(E2; 0_{\rm gs}^+ \rightarrow 2_1^+)$ is in agreement with this experimental value is somewhat surprising. Let us mention that a recent measurement [52] gives a much larger value $B(E2; 0_{\rm gs}^+ \rightarrow 2_1^+)$=602 (82) $e^2\,\mathrm{fm}^4$.

A deformed GS for ^{32}Mg is consistent with the results of Poves and Retamosa [11,14] who stress the role of intruder states in the onset of deformation near $N = 20$ far from stability. Our results are also consistent with the results of Otsuka [15] who concludes that ^{32}Mg looks like a γ-unstable deformed nucleus. As can be seen in fig. 16, the 0^+ and 2^+ collective wave functions contain large components of non-axial configurations.

3.2.2 The ^{44}S nucleus

Figure 17 shows the PES of ^{44}S in the β-γ plane (right part) and in axial symmetry (left part), with ZPE corrections included. A comparison with fig. 10 shows that the effect of ZPE corrections is to increase the depth of both oblate and prolate minima. The energies and β-γ deformations of the first excited states are indicated as in fig. 15. As in ^{32}Mg, the GS energy is large enough for the GS wave function to be a mixing of prolate, oblate and intermediate gamma deformations, so the first 0^+, 2^+, and 4^+ states are triaxial with $\langle\gamma\rangle \simeq 30°$. In fact, the first 0^+ collective wave function represented in fig. 18 shows that the GS is triaxial with a maximum near $\beta = 0$. In the same figure, one can see that, in contrast to the GS one, the 2^+ collective wave function is peaked at a prolate deformation $\beta \simeq 0.25$. Nevertheless, this 2^+ state contains large γ deformation admixtures. Analysis of the K-content of the 2^+ collective wave function yields 83 % for $K = 0$ and 17 % for $K = 2$.

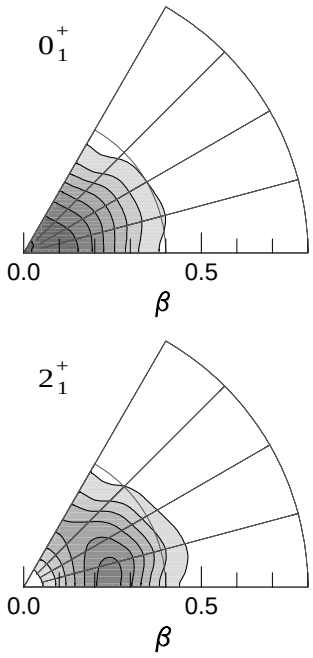

Fig. 18. Collective wave functions in β-γ plane of the first 0^+ and 2^+ collective levels of ^{44}S.

We find the excitation energy of the first 2^+ excited state is 1.46 MeV and the reduced transition probability we calculate is $B(E2; 0^+_{\rm gs} \rightarrow 2^+_1) = 420e^2\,{\rm fm}^4$. These results are in good agreement with the experimental values obtained by Glasmacher *et al.* [25] via intermediate energy Coulomb excitation : $B(E2; 0^+_{\rm gs} \rightarrow 2^+_1)= 314(88)e^2\,{\rm fm}^4$, and $E(2^+) = 1.297$ (0.018) MeV. The experimental β-value deduced by these authors (0.258) is quite large compared to our result (0.2). However, this value has been derived using the prescription of Raman *et al.* [53], which deduces β_2 from the reduced transition probability. Using the same prescription we find $\beta_2 = 0.268$ from our $B(E2; 0^+_{\rm gs} \rightarrow 2^+_1)$. Let us note that GS β deformations ranging from -0.15 to 0.3 are found in the other theoretical models applied to this nucleus [25,27].

4 Conclusion

The microscopic calculations performed in this work with the Gogny effective interaction show that both $N = 20$ and $N = 28$ shell closures vanish in neutron-rich nuclei. This conclusion is in agreement with the results of most other theoretical models, as well as with available experimental observations.

The disappearance of shell closures has been found to stem from different origins in $N = 20$ and $N = 28$ nuclei. In the former case, $N = 20$ always is a spherical magic number of the neutron mean field. The $N = 20$ energy gap remains large in all studied nuclei, decreasing from 7 MeV in ^{40}Ca to 5.4 MeV in ^{30}Ne. However, configuration mixing of HFB solutions is found to have a considerable effect on the structure of these nuclei. Including vibration-rotation coupling yields a deformed GS in ^{32}Mg and, therefore, results in a breaking of the $N = 20$ closure in this nucleus.

In the case of $N = 28$ nuclei, the spherical neutron shell closure is already broken at the mean-field level for $N - Z \geq 10$. As a counterpart, deformed shell closures appear in most nuclei. Configuration mixing also plays an important role in $N = 28$ exotic nuclei. The results obtained for ^{44}S are in remarkable agreement with experiments. They show that the GS and first excited state wave functions of this nucleus contain large admixtures of triaxial components.

From this study, it appears that different mechanisms may exist, leading to the disappearance of shell closures. As exemplified in ^{32}Mg, analyzing this phenomenon in a pure mean-field context may not be sufficient to explore the variety of them. It can be noted in this respect that a configuration mixing of HFB deformed states represents an efficient way of taking into account intruder states, as explicitly done in shell model approaches.

Finally, let us point out that the present study devoted to light nuclei far from stability might suffer from two approximations introduced in the configuration mixing calculations : the Gaussian Overlap Approximation, and the use of Inglis-type vibrational masses. The role played by collective modes other than the quadrupole modes also should be examined. Improvements of the present approach in these directions are left for future work.

We would like to thank J.-P. Delaroche and E. Bauge for their critical reading of the manuscript and useful suggestions.

References

1. O. Haxel, J.H.D. Jensen and H.E. Suess, Phys. Rev. **75**, 1766 (1949); M.G. Mayer, Phys. Rev. **75**, 1969 (1949); M.G. Mayer and J.H.D. Jensen, *Elementary Theory of Nuclear Shell Structure* (Wiley, New York, 1955).
2. X. Campi et al., Nucl. Phys. A **251**,193 (1975).
3. C. Thibault et al., Phys. Rev. C **12**, 644 (1975).
4. D.J. Vieira et al., Phys. Rev. Lett. **57**, 3253 (1986).
5. N.A. Orr et al., Phys. Lett. B **258**, 29 (1991).
6. X.G. Zhou et al., Phys. Lett. B **260**, 285 (1991).
7. M. Baranco and R.J. Lombard, Phys. Lett. B **78**, 542 (1978).
8. C. Detraz et al., Nucl. Phys. A **394**, 378 (1983).
9. D. Guillemaud-Mueller et al., Nucl. Phys. A **426**, 37 (1984).
10. B.H. Wildenthal and W. Chung, Phys. Rev. C **22**, 2260 (1980).
11. A. Poves and J. Retamosa, Phys. Lett. B **184**, 311 (1987).
12. E.K. Warburton, J. A. Becker and B.A. Brown, Phys. Rev. C **41**, 1147 (1990).
13. N. Fukunishi, T. Otsuka and T. Sebe, Phys. Lett. B **296**, 279 (1992).
14. A. Poves and J. Retamosa, Nucl. Phys. A **571**, 221 (1994).
15. Takaharu Otsuka, Nucl. Phys. A **616**, 406c (1997).

16. E. Caurier, F. Nowacki, A. Poves and J. Retamosa, Phys. Rev. C **58**, 2033 (1998).
17. S.K. Patra and C.R. Praharaj, Phys. Lett. B **273**, 13 (1991).
18. Zhongzhou Ren, Z.Y. Zhu, Y.H. Cai and Gongou Xu, Phys. Lett. B **380**, 241 (1996).
19. G.A. Lalazissis, A.R. Farhan and M.M. Sharma, Nucl. Phys. A **628**, 221 (1998).
20. J. Terasaki, H. Flocard, P.H. Heenen and P. Bonche, Nucl. Phys. A **621**, 706 (1997).
21. R. Rodriguez-Guzman, J.L. Egido and L.M. Robledo, Phys. Lett. B **474**, 15 (2000).
22. P. Moller, J. R. Nix, W. D. Myers and W. J. Swiatecki, At. Data Tables **59**, 185 (1995).
23. O. Sorlin et al., Phys. Rev. C **47**, 2941 (1993).
24. O. Sorlin et al., Nucl. Phys. A **587**, 763 (1995).
25. T. Glasmacher et al., Phys. Lett. B **395**, 163 (1997).
26. D. Hirata, K.Sumiyoshi, B. V. Carlson, H. Toki and Tanihata, Nucl. Phys. A **609**, 131 (1996).
27. T.R. Werner et al., Nucl. Phys. A **597**, 327 (1996).
28. T.R. Werner et al., Phys. Lett. B **333**, 303 (1994); T.R. Werner et al., Phys. Lett. B **335**, 259 (1994).
29. G.A. Lalazissis et al., Phys. Rev. C **60**, 014310 (1999).
30. J. Retamosa, E. Caurier, F. Nowacki and A. Poves, Phys. Rev. C **55**, 1266 (1997).
31. J.-F. Berger et al., *Proceeding of the Sixth International Conference on Nuclei Far From Stability* and *Ninth International Conference on Atomic Masses and Fundamental Constants, Bernkastel-Kues, Germany, 19-24 July, 1992* edited by R. Neugart and A. Wöhr, IOP Conf. Proc. **132** (IOS Publishing, Bristol, 1993) p. 487.
32. J. Dechargé and D. Gogny, Phys. Rev. C **21**, 1568 (1980).
33. J.F. Berger, M. Girod and D. Gogny, Nucl. Phys. A **502**, 85c (1989).
34. J. Dobaczewski, H. Flocard and J. Treiner, Nucl. Phys. A **422**, 103 (1984).
35. M. Girod and B. Grammaticos, Phys. Rev. C **27**, 2317 (1983).
36. J.F. Berger, M. Girod and D. Gogny, Comp. Phys. Comm. **63**, 365 (1991).
37. M. Girod, Ph. Dessagne, M. Bernas, M. Langevin, F. Pougheon and P. Roussel, Phys. Rev. C **37**, 2600 (1988); M.C. Mermaz and M. Girod, Phys. Rev. C **53**, 1819 (1996); C. Gautherin et al., Eur. Phys. J. A **1**, 391 (1998); F. Le Blanc et al., Phys. Rev. C **60**, 054310 (1999); F. Maréchal et al., Phys. Rev. C **60**, 034615 (1999).
38. O. Tarasov et al., Phys. Lett. B **409**, 64 (1997).
39. P.D. Cottle and K. W. Kemper, Phys. Rev. C **58**, 3761 (1998).
40. P. Ring and P. Schuck, *The Nuclear Many-Body Problem* (Springer, Berlin, 1980) p. 398.
41. D.L. Hill and J.A. Wheeler, Phys. Rev. **89**, 1102 (1953); J.J. Griffin and J.A. Wheeler, Phys. Rev. **108**, 311 (1957).
42. D.H. Schiff and B. Jancovici, Nucl. Phys. **58**, 678 (1964); A. Kamlah, Z. Phys. **216**, 52 (1968); F.M.H. Villars, in *Procedings of the International Conference on Nuclear Selfconsistent Field, Trieste, 1975*, edited by G. Ripka and M. Porneuf (North-Holland, Amsterdam, 1975).
43. J. Libert, M. Girod and J.-P. Delaroche, Phys. Rev. C **60**, 054301 (1999).
44. M. Girod and B. Grammaticos, Nucl. Phys. A **330**, 40 (1979).
45. D. R. Inglis, Phys. Rev. **103**, 1786 (1956).
46. M. Girod, J.-P. Delaroche, J.-F. Berger and J. Libert, Phys. Lett. B **325**, 1 (1994).
47. K. Kumar and M. Baranger, Nucl. Phys. A **92**, 608 (1967).
48. K. Kumar in *The Electromagnetic Interaction in Nuclear Spectroscopy*, edited by W.D. Hamilton, (North-Holland, Amsterdam 1975), p. 55, and references therein.
49. E. Kh. Yuldashbaeva, J. Libert, P. Quentin and M. Girod, Phys. Lett. B **461**, 1 (1999).
50. T. Motobayashi et al., Phys. Lett. B **346**, 9 (1995).
51. B. V. Pritychenko et al., Phys. Lett. B **461**, 322 (1999).
52. A. Gillibert et al., private communication and to be published.
53. S. Raman et al., Phys. Rev. C **43**, 556 (1991).